A Journal of the Gesellschaft Deutscher Chemiker

Angewandte International Edition GDCh Chemie

www.angewandte.org

## Accepted Article

**Title:** Machine-Learning-Assisted Selective Synthesis of Semiconductive Silver Thiolate Coordination Polymer with Segregated Paths for Holes and Electrons

**Authors:** Takuma Wakiya, Yoshinobu Kamakura, Hiroki Shibahara, Kazuyoshi Ogasawara, Akinori Saeki, Ryosuke Nishikubo, Akihiro Inokuchi, Hirofumi Yoshikawa, and Daisuke Tanaka



**To be cited as:** *Angew. Chem. Int. Ed.* 10.1002/anie.202110629

**Link to VoR:** https://doi.org/10.1002/anie.202110629

WILEY-VCH

10.1002/anie.202110629

RESEARCH ARTICLE

WILEY-VCH

# Machine-Learning-Assisted Selective Synthesis of Semiconductive Silver Thiolate Coordination Polymer with Segregated Paths for Holes and Electrons

Takuma Wakiya,[a] Yoshinobu Kamakura,[a] Hiroki Shibahara,[a] Kazuyoshi Ogasawara,[a] Akinori Saeki,[b] Ryosuke Nishikubo,[b] Akihiro Inokuchi,[c] Hirofumi Yoshikawa[d] and Daisuke Tanaka*[,a,e]

[a] T. Wakiya, Dr. Y. Kamakura, H. Shibahara, Prof. K. Ogasawara, Prof. D. Tanaka
Department of Chemistry
School of Science and Technology
Kwansei Gakuin University
2-1 Gakuen, Sanda, Hyogo 669-1337, Japan
*E-mail: dtanaka@kwansei.ac.jp

[b] Prof. A. Saeki, Dr. R. Nishikubo
Department of Applied Chemistry
Graduate School of Engineering
Osaka University
2-1 Yamadaoka, Suita, Osaka 565-0871, Japan

[c] Prof. A. Inokuchi
Department of Informatics
School of Science and Technology
Kwansei Gakuin University
2-1 Gakuen, Sanda, Hyogo 669-1337, Japan

[d] Prof. H. Yoshikawa
Department of Nanotechnology for Sustainable Energy
School of Science and Technology
Kwansei Gakuin University
2-1 Gakuen, Sanda, Hyogo 669-1337, Japan

[e] Prof. D. Tanaka
JST PRESTO
2-1 Gakuen, Sanda, Hyogo 669-1337, Japan

Supporting information for this article is given via a link at the end of the document.

**Abstract:** Coordination polymers (CPs) with infinite metal–S bond networks have unique electrical conductivities and optical properties, thus drawing attention. However, the development of new $(-M-S-)_n$-structured CPs is hindered by their crystallization difficulty. Herein, we use machine learning to optimize the synthesis of trithiocyanuric acid ($H_3ttc$)-based semiconductive CPs with infinite Ag–S bond networks, report three CP crystal structures, and reveal that isomer selectivity is mainly determined by proton concentration in the reaction medium. One of the CPs, $[Ag_2Httc]_n$, features a 3D extended infinite Ag–S bond network with 1D columns of stacked triazine rings, which, according to first-principle calculations, provide separate paths for holes and electrons. Time-resolved microwave conductivity experiments show that $[Ag_2Httc]_n$ is highly photoconductive ($\varphi\Sigma\mu_{max} = 1.6 \times 10^{-4}$ cm$^2$ V$^{-1}$ s$^{-1}$). Thus, our method promotes the discovery of novel CPs difficult to crystallize with selective topologies.

## Introduction

Coordination polymers (CPs) and metal–organic frameworks (MOFs) exhibit the features of both inorganic and organic compounds are therefore of particular interest.[1] Various CPs and MOFs with coordinated S have been recently reported,[2] including those featuring infinite metal–S $(–M–S–)_n$ bonds arranged in one-dimensional chains,[3] two-dimensional layers,[4] and three-dimensionally extended structures.[5] Such materials exhibit high electrical conductivities and structural stabilities, thus finding numerous applications in electronic devices.[6] However, CPs and MOFs with metal–thiolate bonds often exhibit poor crystallinities, mainly because of the strong M–S bonds and the rapid precipitation of low-crystalline solids, and are therefore difficult to obtain as single crystals.[2f] Furthermore, the large ionic radius of S allows this element to adopt different bridging ($\mu$) modes, which results in the broad structural diversity of the corresponding CPs and MOFs.[7] Moreover, the flexibility of the S coordination geometry makes the control of the topological isomers of M–S CPs and MOFs important for their crystal structure design.[8] Therefore, facile and versatile methods for optimizing the syntheses of highly crystalline CPs and MOFs with metal–thiolate bonds are highly sought after.[2f]

Recently, machine learning applications have rapidly expanded in the area of materials science[9] and have been used to optimize syntheses.[10] However, reports on the application of machine learning to the preparation of novel CPs and MOFs are few because of the complicated compositions of the solids obtained in failure experiments. The products obtained during such optimization procedures are often complex mixtures, and a facile approach for the assessment of such crude products is yet to be established.

We have recently reported a method allowing one to explore the synthetic conditions of novel MOFs based on two machine learning techniques, namely (i) the cluster analysis of powder X-ray diffraction (PXRD) patterns and (ii) random forest and decision tree analysis.[11] Cluster analysis is an unsupervised learning technique automatically grouping the PXRD patterns of crystals obtained under various synthetic conditions based on the degree of similarity (correlation) between these patterns. Random forest and decision tree analysis are supervised learning techniques that create a prediction model using the experimental conditions as explanatory variables and the PXRD patterns classified by clustering analysis as objective variables. The above approach allowed us to extract chemical insights from failure experiments and optimize the conditions for the synthesis of novel MOFs. Herein, this method is applied to the

syntheses of novel Ag–S CPs (Figure 1), which have attracted much attention because of their unique optical properties and semiconducting nature.[4b, 12] Specifically, we describe the syntheses and crystal structures of three novel topological isomers of CPs comprising $Ag^+$ and trithiocyanuric acid ($H_3ttc$). The dominant reaction parameters for selective isomer syntheses are determined through the machine-learning-based analysis of failure experiments, and the optimal isomer is shown to exhibit favorable photoconductivity.

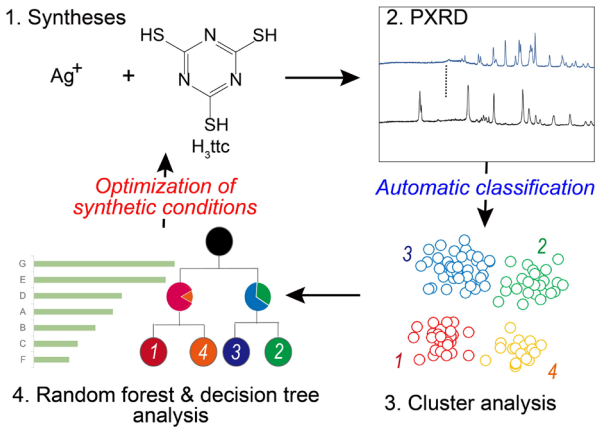


**Figure 1.** Schematic application of machine learning to the selective syntheses of novel Ag–S coordination polymers.

## Results and Discussion

### First exploratory synthesis and machine-learning-based analysis for 114 synthetic conditions

Initially, we searched for conditions under which $Ag^+$ and $H_3ttc$ form crystalline CPs. Specifically, the CPs were synthesized using different temperatures (45–130 °C), solvents (acetone, water, dimethylformamide, dimethyl sulfoxide, acetonitrile, and their mixtures), metal ion/ligand ratios (0.25–4 mol/mol), reaction times (48–108 h), metal ion and ligand concentrations (1.6–300 mM), and reaction containers (screw cap glass tube or Teflon autoclave). Overall, 114 conditions were tested. Although we intended to fabricate single crystals, only powdered crystals unsuitable for single-crystal structural analysis were obtained. Therefore, we attempted to extract chemical insights from failure experiments. As precipitates were obtained under all conditions, they were collected by centrifugation and analyzed by PXRD, which revealed the presence of single-phase $Ag_2S$, a low-crystalline phase, an unknown phase, or complicated mixtures. To analyze the experimental data using supervised machine learning, one must define what phases correspond to successful results. However, arbitrariness was inevitable when the PXRD patterns of these mixtures were assessed by humans to determine reaction success/failure, and thus, an objective approach was necessary. Therefore, we performed cluster analysis to automatically classify the PXRD patterns into several categories based on similarities (Figure S1, Supporting Information) and further verified placement accuracy on a point-by-point basis. The patterns were classified into five categories, namely two unknown phases [**unknown phase 1** (23 cases) and **unknown phase 2** (7 cases)], a low-crystalline phase (56 cases), $Ag_2S$ (27 cases), and a minor uncertain impurity phase (1 case) (Figures 2(a) and S1). At this point, we want to re-state that the grouping of PXRD patterns into one of the five categories by humans is inevitably arbitrary, whereas clustering analysis forces each pattern into one of the categories using quantitative indicators, which is one of the advantages of this analysis. As the following supervised learning handles data statistically, one can expect blurring in the boundary region not to be a fatal problem.

Random forest analysis was subsequently performed to evaluate the main reaction parameters affecting product selectivity (Section S4). The 10 synthetic parameters, namely reaction temperature, solvent type, reaction container type, ligand concentration, metal/ligand ratio, metal ion concentration, isothermal reaction time (h), modulator type, modulator amount (mol), and modulator concentration (mM), were used as explanatory variables. Temperature, concentration, reaction time, and mixing ratio were expressed as numerical data, whereas solvent type, modulator type, and reaction container type, which are difficult to handle as numerical data, were expressed as categorical data. The main phase determined by cluster analysis of PXRD patterns for different conditions was analyzed as an objective variable. The results of random forest analysis allowed the number of explanatory variables with large contributions to be decreased to eight, namely reaction temperature (contribution = 30.3%), solvent type (28.6%), reaction container type (11.7%), ligand concentration (11.0%), metal/ligand ratio (9.5%), metal ion concentration (7.3%), isothermal reaction time (0.9%), and modulator amount (0.4%) (Figure S4). For visualization, decision tree analysis was performed using the screened explanatory variables. Figure 2(b) shows the decision tree based on the dataset containing 114 synthetic conditions and the corresponding PXRD patterns, indicating that $Ag_2S$ mainly forms above 120 °C. This behavior strongly suggests that high temperatures induce the decomposition of $H_3ttc$. In most cases, the addition of water as a solvent led to $Ag_2S$ formation, which suggests that $H_3ttc$ is hydrolyzed at high temperatures to produce $H_2S$. Although we did not consider the possibility of this hydrolysis taking place prior to carrying out decision tree analysis, $H_3ttc$ has been reported to gradually produce $H_2S$ in water at high temperatures by aromatic nucleophilic substitution–based hydrolysis (Figure S8),[13] which can be enhanced by $Ag^+$ coordination.[14a, 14b] Therefore, decision tree analysis indicated the importance of preventing hydrolysis and suggested that **unknown phases 1** and **2** are more likely to form under the conditions in the lower right branch of the decision tree. In summary, we inferred that $Ag_2S$ is more likely to form at temperatures above 120 °C, while unknown phases tend to form in the presence of water or acetonitrile, and the low-crystalline phase easily forms in the absence of water. On the other hand, the reaction container type did not appear on the decision tree node, although random forest analysis suggested that this parameter affected the reaction outcome (score = 11.7%, see Figure S4). This discrepancy was explained as follows. All experiments using screw cap glasses were conducted at low temperatures (≤70 °C) in view of the low resistance of these glasses to pressure. The *p*-value of logistic regression with "temperature," as the explanatory variable, and "reaction container type," as the objective variable, was below 0.0001, indicating a strong correlation between temperature and reaction container type. Therefore, it is most likely that the

container type and the experimental results were indeed associated but not causally related, i.e., their relationship was spurious. In this case, temperature would be the originally dominant factor. Indeed, random forest analysis showed that temperature had the highest contribution of 30.3% (Figure S4).

**Second exploratory synthesis and machine learning analysis for 326 synthetic conditions**

We performed 212 additional experiments to synthesize single crystals of **unknown phases 1** and **2**. Based on the results of decision tree analysis, the reaction temperature was set below 100 °C to avoid ttc hydrolysis, and water- or acetonitrile-containing solvents were used. As container type did not appear to be a dominant factor in the nodes of the decision tree in Figure 2(b), all additional experiments were conducted using Teflon containers. We also focused on certain parameters with low (according to random forest analysis) contributions. The low contribution of a given parameter not only suggests that it cannot influence the experimental results, but also implies that the range of the explored experimental conditions may have been too narrow to contribute. For this reason, parameters with contributions evaluated as low by random forest analysis should not be ignored but rather be expanded to the currently unexplored conditions. For example, in 114 experiments, we added a monodentate ligand (acetic acid) as a modulator to improve crystallinity.[15] The results of random forest analysis performed for the 114 conditions indicated that the contribution of the modulator was small. However, as the addition of acetic acid was only examined under four conditions, it was impossible to determine whether modulators actually play an important role in determining product selectivity. Therefore, we performed additional experiments using various modulator types [acetic acid (AcOH), benzoic acid (HBA), sodium *N*,*N*-diethyldithiocarbamate (DDC), pyridine (Pyr), diethylamine (DEA), triethylamine (TEA), ethylenediamine (EDA)] and concentrations (Figure S9). While no single crystals of **unknown phases** were obtained, the 326 conditions were subjected to cluster analysis, random forest analysis, and decision tree analysis (Figures 2(c), S2, S5, and S7). The patterns were again classified into five categories, namely **unknown phase 1** (63 cases), **unknown phase 2** (19 cases), a low-crystalline phase (175 cases), $Ag_2S$ (61 cases), and a minor uncertain impurity phase (8 cases) (Figure S2). According to cluster analysis, four patterns fell into a category different from that assigned by analysis of the 114 conditions. These four entries were PXRD patterns of mixtures of two or more phases (Figure S3). The number of cases where the classification differed from that observed for 114 conditions was relatively small, which demonstrated the good reproducibility of cluster analysis.

The results of decision tree analysis (Figures 2(c) and S6) indicated that $Ag_2S$ formed in the presence of water above 90 °C. Below 90 °C, **unknown phase 2** was obtained in the presence of AcOH and HBA as modulators. In contrast, the low-crystalline phase was mainly obtained in non-aqueous solvents or at high concentrations of Pyr, EDA, DEA, or TEA. **Unknown phase 1** was predominantly obtained when water was used as the solvent in the presence of a moderate modulator amount, which suggested that proton concentration had a significant effect on product selectivity. The information extracted from decision trees revealed the conditions most likely to yield each phase. Specifically, $Ag_2S$ formed in the presence of water at high temperature; **unknown phase 1** formed in the presence of water under weakly basic to acidic conditions; **unknown phase 2** formed in the presence of water under acidic conditions; and the low-crystalline phase formed under basic conditions or in the absence of water. These results suggested that proton concentration is an important factor for the selective syntheses of the unknown phases.

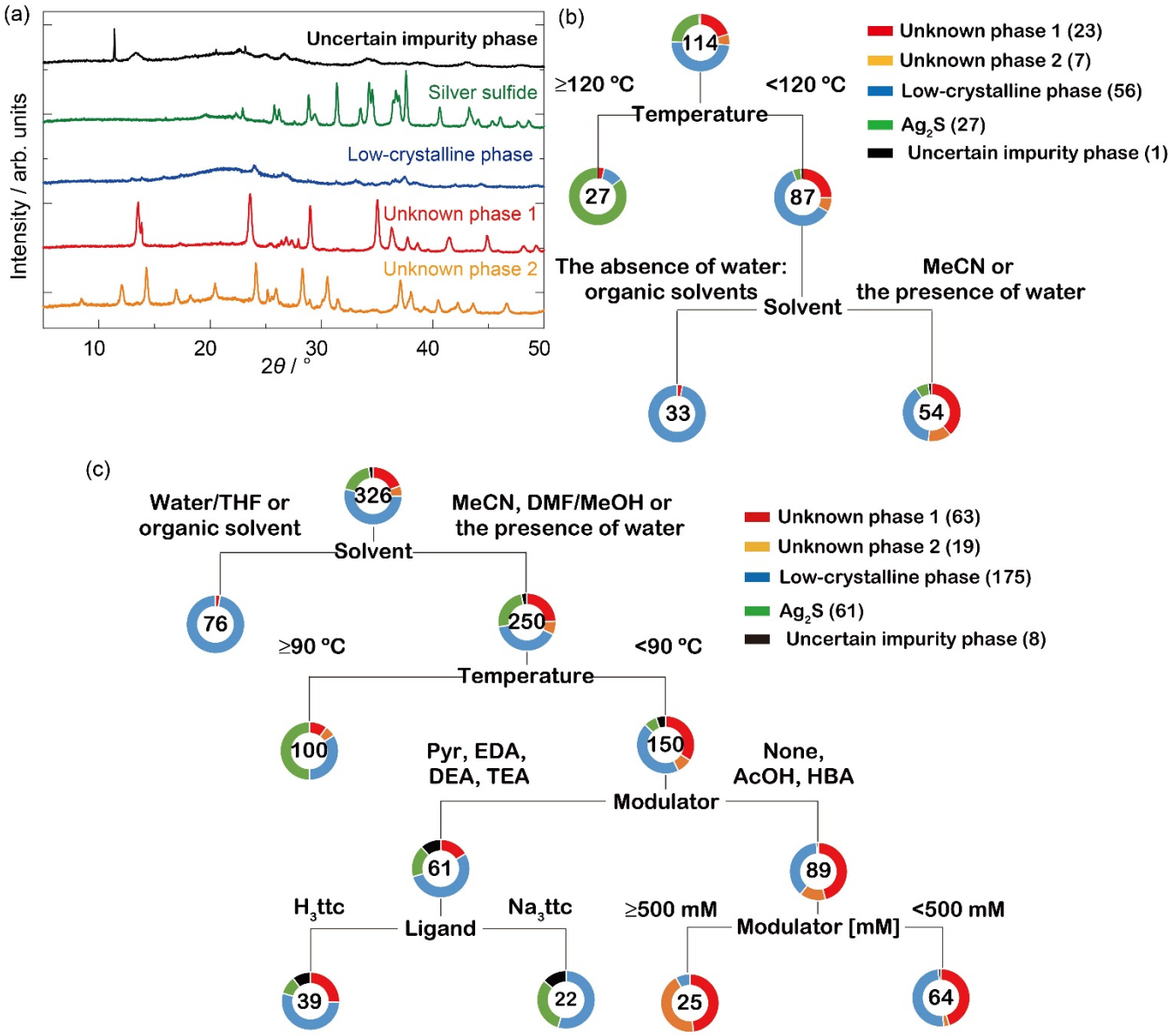


**Figure 2.** (a) Representative powder X-ray diffraction patterns for various categories. Decision trees based on these patterns and (b) 114 or (c) 326 synthetic conditions. The entireties of the corresponding decision trees are shown in Figures S6 and S7, respectively.

**Preparation of single crystals and structural analysis**

According to the random forest analysis of 326 conditions, the contribution of metal ion type was small (2.0%, Figure S5), possibly because only two $Ag^+$ sources were explored, i.e., the influence of the $Ag^+$ source could not be sufficiently evaluated. Therefore, we used insoluble silver halides and successfully obtained single crystals of unknown phases mixed with the silver halide precursors. The formation of large single crystals was most likely due to the deceleration of Ag–S bond formation caused by the sustained release of $Ag^+$ from the insoluble silver halides.[16] As machine learning analysis was not performed with crystal size as the objective variable, the formation of single crystals in the presence of silver halides was an accidental result. However, to get a result different from that of previous experiments, the guideline of exploring a wider range of parameters with small (according to random forest analysis) contributions proved to be useful. Although the products were obtained as mixtures with silver halides, their crystal structures could still be determined (Table 1), which allowed us to validate the results of decision tree analysis as follows.

The composition of **unknown phase 1** (KGF-6) was determined as $[Ag_2Httc]_n$, i.e., one proton was present per ttc unit, in line with the moderate proton concentration used for the synthesis of this phase, as suggested by decision tree analysis. The Ag atoms of KGF-6 were shown to feature an unusual five-fold coordination in a trigonal bipyramidal structure (the N atoms of the triazine ring were not coordinated), with the Ag ions disordered along the axial direction of this structure (Figures 3(a) and S10). The Ag–S bond lengths in the triplanar structure were obtained as 2.50–2.66 Å, and those between the Ag and axial S

atoms were determined as 2.77–3.35 Å (this Ag atom was disordered over three positions). In addition, the Httc ligand was revealed to have two crystallographically non-equivalent S atoms, S1 ($\mu_2$-S atom) and S2 ($\mu_4$-S atom), which could coordinate Ag ions to afford a AgS layer in the *ac*-plane (Figure 3(b)). Furthermore, the layers were stacked with S atoms as shared vertices to form a three-dimensional Ag–S network (Figure 3(d)). Moreover, one-dimensional channels were present between the AgS layers, where the Httc triazine rings aligned perpendicularly to the channel direction to form a one-dimensional columnar structure (Figure 3(c)). The distance between the neighboring C and N atoms in the triazine rings was determined as ~3.09 Å, indicating strong aromatic interactions. Such a columnar structure is also expected to act as an electron carrier path.[17]

**Table 1**. Crystallographic data for KGF-6, -7, and -8.

| Compound | KGF-6 | KGF-7 | KGF-8 |
|---|---|---|---|
| CCDC number | 2052285 | 2052284 | 2071617 |
| Formula | $C_3HAg_2N_3S_3$ | $C_3H_2AgN_3S_3$ | $C_3Ag_3N_3S_3$ |
| Formula weight/Da | 390.99 | 284.13 | 497.85 |
| Temperature/K | 150 | 150 | 150 |
| Crystal system | orthorhombic | monoclinic | orthorhombic |
| Space group | *Pnma* | *C2/m* | $Pna2_1$ |
| *a*/Å | 6.9154(2) | 7.080(4) | 7.5715(10) |
| *b*/Å | 13.0731(4) | 12.924(7) | 7.9093(7) |
| *c*/Å | 7.4840(2) | 7.431(4) | 12.5668(13) |
| *α*/° | 90 | 90 | 90 |
| *β*/° | 90 | 103.196(6) | 90 |
| *γ*/° | 90 | 90 | 90 |
| Volume/Å$^3$ | 676.60(3) | 661.9(7) | 752.57(14) |
| *Z* | 4 | 4 | 4 |
| $\rho_{calc}$/g cm$^{-3}$ | 3.838 | 2.851 | 4.394 |
| $\mu$/mm$^{-1}$ | 6.627 | 3.898 | 8.488 |
| *F*(000) | 728.0 | 544.0 | 912.0 |
| Reflections collected | 21245 | 3541 | 6764 |
| Unique reflections | 807 | 732 | 2158 |
| Goodness-of-Fit on $F^2$ | 1.253 | 0.994 | 1.008 |
| Final $R_1$ index [$I \geq 2\sigma(I)$] | 0.0263 | 0.0246 | 0.0710 |
| Final $R_1$ index [all data] | 0.0276 | 0.0255 | 0.1179 |
| Final $wR_2$ index [$I \geq 2\sigma(I)$] | 0.0815 | 0.0637 | 0.1916 |
| Final $wR_2$ index [all data] | 0.0807 | 0.0629 | 0.1625 |

The composition of **unknown phase 2** (KGF-7) was determined as $[AgH_2ttc]_n$, i.e., two protons were present per ttc unit (Figures 3(e) and S11). The two Ag atoms formed Ag–S bonds (2.52–2.88 Å) with the four $H_2$ttc S atoms to afford a dinuclear complex connected by $H_2$ttc units, i.e., a one-dimensional CP. The presence of one proton in KGF-6 and two protons in KGF-7 agreed with the tendency of KGF-6 to form under near-neutral conditions and that of KGF-7 to form under acidic conditions, as suggested by the decision trees. Furthermore, a single crystal of proton-free $[Ag_3ttc]_n$ (KGF-8) was accidentally prepared in the presence of 4,4'-bipyridine (bpy). Although the temperature factor could not be optimized, and the electron density around the Ag atoms was high because of the poor quality of the KGF-8 single crystal, the simulated PXRD pattern of this CP agreed well with the broad PXRD patterns of some samples classified as the low-crystalline phase (Figure S13). The formation of proton-free single-crystalline KGF-8 was ascribed to the action of bpy as a good proton acceptor. The fully deprotonated structure of ttc in KGF-8 well agreed with the decision tree results, showing that the low-crystalline phase was more likely to form under basic or water-free conditions, i.e., at low proton concentrations. KGF-8 also featured Ag–Ag and Ag–N bonds, unlike KGF-6 and -7 (Figures 3(f) and S12). KGF-6 and -7 were stable in water and 0.1 M HCl for 24 h, but were deprotonated to afford KGF-8 when immersed into 0.1 M NaOH (Figure S14). Thermogravimetric analysis revealed that KGF-6, -7, and -8 are stable up to 300 °C (Figure S15), confirming the thermal and chemical stabilities of these thiolate-coordination-based CPs.

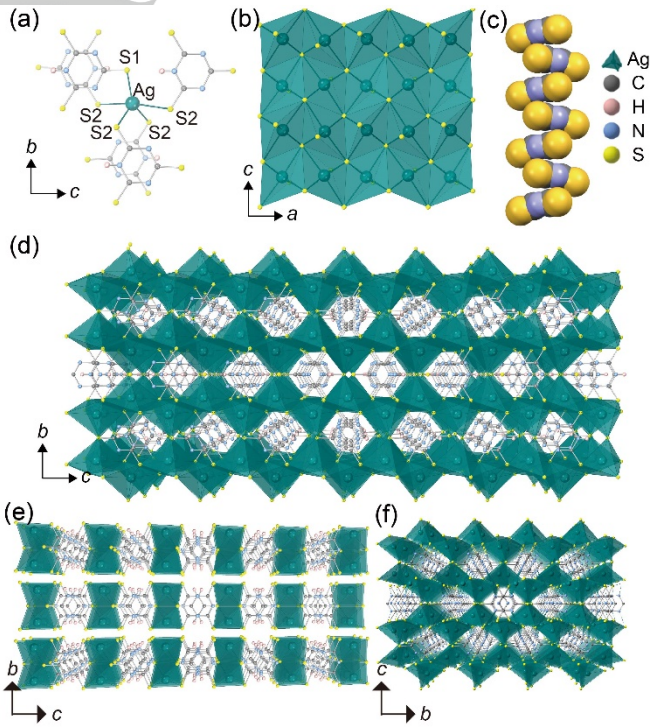


**Figure 3.** (a) Ligand coordination environment of $[Ag_2Httc]_n$ (KGF-6). (b) Portion of KGF-6 structure along the *b*-axis. (c) One-dimensional column of Httc molecules in KGF-6. (d) Perspective view of the KGF-6 crystal structure along the *a*-axis. (e) Perspective view of the $[AgH_2ttc]_n$ (KGF-7) crystal structure along the *a*-axis. (f) Perspective view of the $[Ag_3ttc]_n$ (KGF-8) crystal structure along the *a*-axis. Ag: green, S: yellow, N: blue, C: gray, H: pink. The displayed Ag atoms represent the major occupancy.

**Evaluation of electronic properties**

Based on the diffuse reflectance ultraviolet-visible-near-infrared spectra of KGF-6, -7, and -8, their optical bandgaps were determined as 2.76, 2.79, and 2.95 eV, respectively (Figure S19). Photoelectron yield spectra revealed that the valence band maximum (VBM) levels of all three isomers were nearly identical, equaling −5.92, −5.98, and −5.93 for KGF-6, -7, and -8, respectively (Figures S20 and S21). The band structures and densities of states of each isomer were evaluated using CASTEP first-principle calculations,[18] and the VBM and conduction band minimum (CBM) of KGF-7 and -8 were found to be relatively flat. Contrastingly, KGF-6 exhibited a steeply dispersed band structure with VBM and CBM levels of ~0.4 eV (Figures 4(a), (c), and (e)), which indicated semiconductor-like behavior. The effective masses of holes and electrons were obtained by density functional theory calculations as $m_h^* = 0.96m_0$ and $m_e^* = 0.81m_0$ ($m_0$ = electron rest mass), respectively, and were therefore comparable to those of a previously reported highly-conductive MOF, $Fe_3(THT)_2(NH_4)_3$ (THT = 2,3,6,7,10,11-triphenylenehexathiol), which was claimed to have a mobility as high as ~220 $cm^2 V^{-1} s^{-1}$.[19] Notably, the VBM and CBM of KGF-6 mainly originated from the Ag and S atoms and the C and N atoms, respectively (Figure 4(b)). Furthermore, the highest occupied molecular orbital and lowest unoccupied molecular orbital distributions indicated that these orbitals are distributed across the AgS network and the triazine ring, respectively (Figure S22), to form an alternating *p–n* heterostructure at the molecular level for charge separation. The segregated structure and the relatively low effective masses of holes and electrons could provide ambipolar pathways, which may be a useful attribute in the context of photocatalysis and solar cells. Moreover, time-resolved microwave conductivity (TRMC) measurements were performed to evaluate the CP photoconductivities. The maximum values of $\varphi\Sigma\mu_{max}$ ($\varphi$ = charge carrier generation yield, $\Sigma\mu$ = sum of hole and electron mobilities) equaled $1.6 \times 10^{-4}$, $2.7 \times 10^{-5}$, and $2.8 \times 10^{-5}$ $cm^2 V^{-1} s^{-1}$ for KGF-6, -7, and -8, respectively (Figure 5). The value obtained for KGF-6 is one order of magnitude higher than those of KGF-7 and -8 and is comparable to those of previously reported conductive CPs, MOFs, and covalent organic frameworks.[20] The TRMC results were consistent with the band dispersions (flat for KGF-7 and -8; steeper for KGF-6) obtained by first-principle calculations. The effective lifetime (i.e., the weight-averaged lifetimes of double-exponential fits) of KGF-6 was determined as 10.2 μs; thus, this compound exhibited both a long-lived charge separation state and high mobility. This finding was consistent with the crystal structure having segregated paths for hole and electron transport.[21] With decreasing excitation intensity (~$10^{16}$–$10^{14}$ photon $cm^{-2}$ $pulse^{-1}$), $\varphi\Sigma\mu_{max}$ slightly increased, but the half-life times decreased, which suggests that charge carrier decay was mainly due to charge trapping (Figure S26).

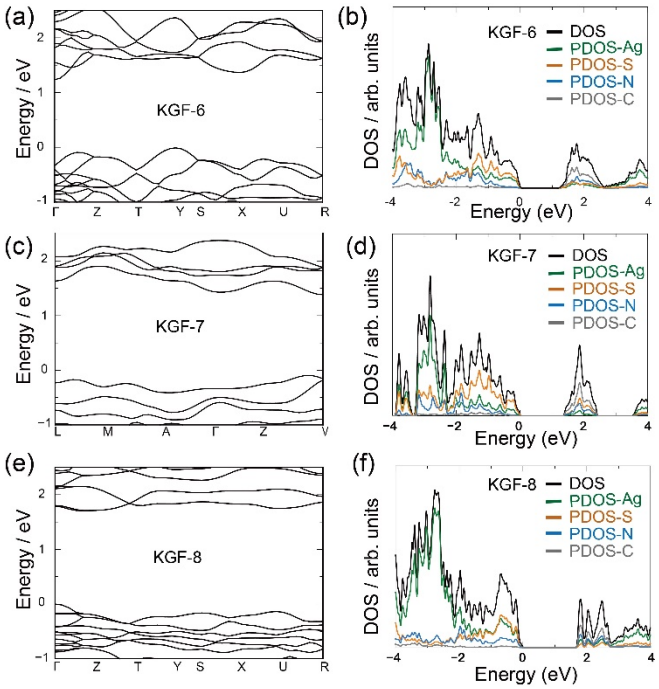


**Figure 4.** (a, c, e) Band structures and (b, d, f) density of states of (a, b) KGF-6, (c, d) KGF-7, and (e, f) KGF-8. In the band structures, the energy level of the valence band maximum is represented as zero.

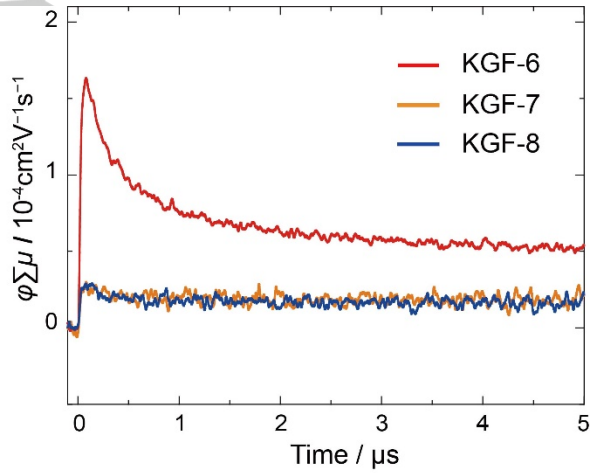


**Figure 5.** Results of time-resolved microwave conductivity measurements ($\lambda_{ex}$ = 355 nm) for KGF-6 (red), KGF-7 (orange), and KGF-8 (blue).

## Conclusion

Semiconductive CPs containing Ag–S bonds were synthesized using machine learning to extract chemical insights from failure experiments. Single-crystal structure analysis demonstrated that the number of protons in the isomer crystal structures was consistent with the proton concentration dependency in the synthetic conditions suggested by decision tree analysis. One topological isomer, KGF-6, possessed an infinite three-dimensional Ag–S network and a one-dimensional columnar triazine ring structure, therefore exhibiting high photoconductivity, as evidenced by first-principle calculations and TRMC measurements. The proposed machine-learning-assisted

method is expected to promote the discovery of novel CPs that are difficult to crystallize with selective topologies.

## Acknowledgements

This work was supported by JST PRESTO (Grant Nos. JPMJPR15N6, JPMJPR17NA) and JSPS KAKENHI (Grant Nos. 20H02577, 20H04680, 20H04646, 20H05836, 17K00320, and 20J13900). We would like to thank Editage (www.editage.com) for English language editing.

**Keywords:** semiconductors • crystal engineering • coordination polymers • machine learning • silver thiolate network

[1] a) L. S. Xie, G. Skorupskii, M. Dinca, *Chem. Rev.* **2020**, *120*, 8536; b) M. O'Keeffe, O. M. Yaghi, *Chem. Rev.* **2012**, *112*, 675; c) S. Kitagawa, R. Kitaura, S. Noro, *Angew. Chem. Int. Ed.* **2004**, *43*, 2334; d) S. L. Griffin, N. R. Champness, *Coord. Chem. Rev.* **2020**, *414*, 213295.

[2] a) X. Li, W. Ma, H. Li, Q. Zhang, H. Liu, *Coord. Chem. Rev.* **2020**, *408*, 213191; b) Y. Liu, D. Huang, M. Cheng, Z. Liu, C. Lai, C. Zhang, C. Zhou, W. Xiong, L. Qin, B. Shao, Q. Liang, *Coord. Chem. Rev.* **2020**, *409*, 213220; c) O. Veselska, A. Demessence, *Coord. Chem. Rev.* **2018**, *355*, 240; d) G. Givaja, P. Amo-Ochoa, C. J. Gomez-Garcia, F. Zamora, *Chem. Soc. Rev.* **2012**, *41*, 115; e) J. Xie, L. Wang, J. S. Anderson, *Chem. Sci.* **2020**, *11*, 8350; f) Y. Kamakura, D. Tanaka, *Chem. Lett.* **2020**, *50*, 523; g) Z. Ji, C. Trickett, X. Pei, O. M. Yaghi, *J. Am. Chem. Soc.* **2018**, *140*, 13618.

[3] a) L. Sun, T. Miyakai, S. Seki, M. Dinca, *J. Am. Chem. Soc.* **2013**, *135*, 8185; b) N. E. Horwitz, J. Xie, A. S. Filatov, R. J. Papoular, W. E. Shepard, D. Z. Zee, M. P. Grahn, C. Gilder, J. S. Anderson, *J. Am. Chem. Soc.* **2019**, *141*, 3940.

[4] a) A. Pathak, J. W. Shen, M. Usman, L. F. Wei, S. Mendiratta, Y. S. Chang, B. Sainbileg, C. M. Ngue, R. S. Chen, M. Hayashi, T. T. Luo, F. R. Chen, K. H. Chen, T. W. Tseng, L. C. Chen, K. L. Lu, *Nat. Commun.* **2019**, *10*, 1721; b) X. Huang, H. Li, Z. Tu, L. Liu, X. Wu, J. Chen, Y. Liang, Y. Zou, Y. Yi, J. Sun, W. Xu, D. Zhu, *J. Am. Chem. Soc.* **2018**, *140*, 15153.

[5] a) Y. Kamakura, P. Chinapang, S. Masaoka, A. Saeki, K. Ogasawara, S. R. Nishitani, H. Yoshikawa, T. Katayama, N. Tamai, K. Sugimoto, D. Tanaka, *J. Am. Chem. Soc.* **2020**, *142*, 27; b) S. Hu, F. Y. Yu, P. Zhang, D. R. Lin, *Dalton Trans.* **2013**, *42*, 7731; c) A. Eichhofer, S. Lebedkin, *Inorg. Chem.* **2018**, *57*, 602.

[6] L. Sun, M. G. Campbell, M. Dinca, *Angew. Chem. Int. Ed.* **2016**, *55*, 3566.

[7] a) D. Li, W. J. Shi, L. Hou, *Inorg. Chem.* **2005**, *44*, 3907; b) R. D. Shannon, *Acta Crystallogr. A* **1976**, *32*, 751.

[8] X. Huang, Y. Qiu, Y. Wang, L. Liu, X. Wu, Y. Liang, Y. Cui, Y. Sun, Y. Zou, J. Zhu, W. Fang, J. Sun, W. Xu, D. Zhu, *Angew. Chem. Int. Ed.* **2020**, *59*, 22602-22609.

[9] a) G. Panapitiya, G. Avendano-Franco, P. Ren, X. Wen, Y. Li, J. P. Lewis, *J. Am. Chem. Soc.* **2018**, *140*, 17508; b) Y. Xie, C. Zhang, X. Hu, C. Zhang, S. P. Kelley, J. L. Atwood, J. Lin, *J. Am. Chem. Soc.* **2020**, *142*, 1475.

[10] a) D. W. Davies, K. T. Butler, J. M. Skelton, C. Xie, A. R. Oganov, A. Walsh, *Chem. Sci.* **2018**, *9*, 1022; b) P. Raccuglia, K. C. Elbert, P. D. Adler, C. Falk, M. B. Wenny, A. Mollo, M. Zeller, S. A. Friedler, J. Schrier, A. J. Norquist, *Nature* **2016**, *533*, 73; c) K. Muraoka, Y. Sada, D. Miyazaki, W. Chaikittisilp, T. Okubo, *Nat. Commun.* **2019**, *10*, 4459; d) S. M. Moosavi, A. Chidambaram, L. Talirz, M. Haranczyk, K. C. Stylianou, B. Smit, *Nat. Commun.* **2019**, *10*, 539.

[11] Y. Kitamura, E. Terado, Z. Zhang, H. Yoshikawa, T. Inose, H. Uji-i, M. Tanimizu, A. Inokuchi, Y. Kamakura, D. Tanaka, *ChemRxiv Preprint* **2020**, DOI: 10.26434/chemrxiv.13490925.

[12] a) R. W. Huang, Y. S. Wei, X. Y. Dong, X. H. Wu, C. X. Du, S. Q. Zang, T. C. W. Mak, *Nat. Chem.* **2017**, *9*, 689; b) R. W. Huang, X. Y. Dong, B. J. Yan, X. S. Du, D. H. Wei, S. Q. Zang, T. C. W. Mak, *Angew. Chem. Int. Ed.* **2018**, *57*, 8560; c) Z. Y. Wang, M. Q. Wang, Y. L. Li, P. Luo, T. T. Jia, R. W. Huang, S. Q. Zang, T. C. W. Mak, *J. Am. Chem. Soc.* **2018**, *140*, 1069.

[13] E. M. Smolin, L. Rapoport, *Chemistry of Heterocyclic Compounds: s-Triazines and Derivatives*, Interscience Publishers, Inc., New York, **1959**.

[14] a) D. Tanaka, S. Masaoka, S. Horike, S. Furukawa, M. Mizuno, K. Endo, S. Kitagawa, *Angew. Chem. Int. Ed.* **2006**, *45*, 4628; b) R. D. Gillard, *Coord. Chem. Rev.* **1975**, *16*, 67.

[15] T. Tsuruoka, S. Furukawa, Y. Takashima, K. Yoshida, S. Isoda, S. Kitagawa, *Angew. Chem. Int. Ed.* **2009**, *48*, 4739.

[16] K. Nakashima, T. Shimizu, Y. Kamakura, A. Hinokimoto, Y. Kitagawa, H. Yoshikawa, D. Tanaka, *Chem. Sci.* **2020**, *11*, 37.

[17] S. S. Park, E. R. Hontz, L. Sun, C. H. Hendon, A. Walsh, T. Van Voorhis, M. Dinca, *J. Am. Chem. Soc.* **2015**, *137*, 1774.

[18] S. J. Clark, M. D. Segall, C. J. Pickard, P. J. Hasnip, M. J. Probert, K. Refson, M. C. Payne, *Z. Kristallogr.* **2005**, *220*, 567.

[19] R. Dong, P. Han, H. Arora, M. Ballabio, M. Karakus, Z. Zhang, C. Shekhar, P. Adler, P. S. Petkov, A. Erbe, S. C. B. Mannsfeld, C. Felser, T. Heine, M. Bonn, X. Feng, E. Canovas, *Nat. Mater.* **2018**, *17*, 1027.

[20] a) A. Saeki, *Polym. J.* **2020**, *52*, 1307; b) T. C. Narayan, T. Miyakai, S. Seki, M. Dinca, *J. Am. Chem. Soc.* **2012**, *134*, 12932; c) X. Ding, X. Feng, A. Saeki, S. Seki, A. Nagai, D. Jiang, *Chem. Commun.* **2012**, *48*, 8952.

[21] S. Wang, T. Kitao, N. Guillou, M. Wahiduzzaman, C. Martineau-Corcos, F. Nouar, A. Tissot, L. Binet, N. Ramsahye, S. Devautour-Vinot, S. Kitagawa, S. Seki, Y. Tsutsui, V. Briois, N. Steunou, G. Maurin, T. Uemura, C. Serre, *Nat. Commun.* **2018**, *9*, 1660.

10.1002/anie.202110629




## Entry for the Table of Contents

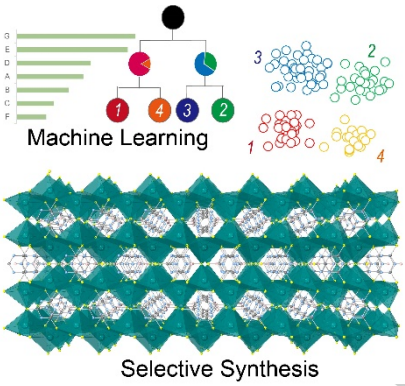


Semiconductive trithiocyanuric acid ($H_3ttc$)-based coordination polymers (CPs) featuring Ag–S bonds are synthesized using machine-learning-assisted techniques. One of the obtained CPs, $[Ag_2Httc]_n$ (KGF-6), contains a three-dimensionally extended infinite Ag–S bond network with one-dimensional column structures of stacked triazine rings, which provides segregated paths for holes and electrons.

Institute and/or researcher Twitter usernames: @DaisukeTanakaKG